https://doi.org/10.1016/j.conbuildmat.2024.135856

Meso-mechanics of packed C-S-H colloids by nanoindentation: A coarse-grained molecular dynamics study

Ming-Feng Kai [a], Jia-Hui Liu [a], Zhuo Tang [b], Jian-Guo Dai [c]

[a] Department of Civil and Environmental Engineering, The Hong Kong Polytechnic University, Kowloon, Hong Kong, China
[b] Department of Civil Engineering, Central South University, Changsha, 410075, China
[c] Department of Architecture and Civil Engineering, City University of Hong Kong, Kowloon, Hong Kong, China

Abstract

Colloidal calcium silicate hydrate (C-S-H) gel significantly contributes to cement paste's strength and durability. In this study, the coarse-grained (CG) models for packed C-S-H colloidal particles with different packing densities were established and meso-mechanically assessed via nanoindentation. Load-depth curves showed indentation hardness values of 0.55, 1.16, and 2.63 GPa for the colloidal systems with packing densities (η) of 0.50, 0.55, and 0.60, respectively. Structurally, the nano-indenter had a broader impact on low-density C-S-H (η = 0.5, impact radius = 118 and 150 nm respectively at indentation depths = 50 and 100 nm) than high-density C-S-H (η = 0.6, impact radius = 106 and 140 nm at the same depths). Low-density colloids were easily compressed without deforming surrounding regions at low depths, while high-density colloids were squeezed laterally, causing deformation in surrounding regions. Packed C-S-H colloids displayed two-stage stress relaxation behavior: rapid initial relaxation due to nanoindentation-induced instability, followed by slower relaxation due to C-S-H's viscous nature. Furthermore, higher loading rates caused initial unstable deformation, but better stability after stress relaxation compared to lower loading cases. However, the effect of loading rate on the impact region was negligible. These meso-level insights enhance our comprehension of the C-S-H gel properties in cement paste as well as the nanoindentation mechanics.

Keywords: C-S-H; Coarse-grained MD; Nanoindentation; Meso-mechanics; Stress relaxation

1. Introduction

Colloidal calcium silicate hydrate (C–S–H) gel, often referred to as the "glue" of cement paste, is a critical component that constitutes over 60% of its volume [1]. This substance plays a pivotal role in determining the chemical, physical, and mechanical properties of the cement paste. Despite extensive research and numerous studies conducted over the years, a comprehensive understanding of C-S-H properties at smaller scales, particularly at the nanoscale and mesoscale, remains a complex and challenging task. The complexity of understanding C-S-H properties stems from a multitude of factors. These include its variable composition (i.e., Ca/Si and H_2O/Si ratios) [2], its layered structure at the nanoscale (i.e., Gennite and Tobermorite) [3], its globular texture at the mesoscale [4], and its multiscale pore structure (i.e., interlayer pore, gel pore, and capillary pore) [5]. These intricate characteristics present significant challenges when investigating the material properties at smaller scales, making it a fascinating yet complex field of study [6].

Over the last decade, nanoindentation has emerged as a specialized technique for measuring localized material properties. This technique, which involves creating indents on the material's surface with a small, rigid tip, has been extensively used to study the microstructural mechanical properties (e.g., indentation modulus M, hardness H, and creep compliance C) of cement paste and cement-based materials, such as nanoparticle-modified cement, carbon nanotube and graphene-modified cement, fibre-reinforced cement, and steel-reinforced concrete [7-9]. Nonetheless, to achieve precise measurements of material properties, meticulous experimental design, accurate data acquisition, and advanced analysis techniques, with particular emphasis on tips, are required to address the inherent limitations associated with nanoindentation measurements, such as the size effect, surface effect, and the influence of indenter geometry. Such experimental efforts are costly and time-consuming [10]. Moreover, the influence of environmental conditions such as temperature and moisture on these properties is hard to measure experimentally, while, at the same time, it is known that these environmental factors can have significant effects on system performance. Conversely, these challenges posed by traditional experimental methodologies can, in general, be effectively addressed through the utilization of atomistic simulations.

Atomistic simulation, a powerful tool that includes first-principles calculations, all-atom molecular dynamics (MD), and coarse-grained MD, can provide direct insights into the nano- and meso-level processes in a material. This approach bypasses the difficulties associated with traditional experimental methods, offering a more efficient and accurate way to study material properties. In 2009, a significant breakthrough was made when Pellenq et al. [11] established the first realistic all-atom model of C-S-H with a chemical composition of $(CaO)_{1.65}(SiO_2)(H_2O)_{1.75}$ using the core-shell potential. This model paved the way for further studies into the structural features, chemical activities, physical characteristics, and mechanical performance of C-S-H's atomic structure. Notably, Hou et al. [12] and Yin et al. [13] conducted MD-based nanoindentation tests to simulate the nano-mechanics the atomic structure of C-S-H, further advancing our understanding of this complex material. In 2016, Ioannidou et al. [14] proposed a series of CG models for C-S-H gel at the mesoscale. These models comprised a pack of colloidal C-S-H colloids, with colloid sizes ranging from 3.78 nm to 9.0 nm and packing fractions between 0.33 and 0.68. The simulations yielded results for scattering intensity, pore size distribution (PSD), surface area, local volume fractions, indentation modulus, and hardness that were in good agreement with experimental data. This provided a quantitative understanding of the elusive mesoscale structure of C-S-H, a significant step forward in the field. Based on Ioannidou's work, several studies were further conducted to capture the mesoscale properties of C-S-H [15-17]. However, to the best of the authors' knowledge, no one has yet performed nanoindentation tests on the mesoscale structure of C-S-H, which is arguably more important compared to the tests on the atomic structure of C-S-H in understanding the macroscale engineering properties.

In this study, the CG models for C-S-H with different packing densities (0.50, 0.55 and 0.60) were established, after which the nanoindentation tests were conducted to measure the meso-mechanical properties of these models. To describe the interactions between the C-S-H colloids, the cohesive-frictional force field (CFFF) was employed. The load-depth curves were recorded for all the colloidal C-S-H systems to gain insights into the meso-mechanical properties during both the loading and unloading processes. Following this, a structural analysis was carried out to evaluate the migration of the colloids and the deformation of local regions during the nanoindentation process. Besides, the stress relaxation of the colloidal C-S-H systems was determined at three constant indentation depths (50, 75 and 100 nm). Finally, the effect of the loading rate on the meso-mechanics of the colloidal C-S-H systems was discussed.

2. Computational Methods

2.1 Force field

In this work, the CFFF, initially proposed by Palkovic et al. [18], was employed to describe the interactions between the mesoscale C-S-H colloids. Different from the generalized Lennard–Jones potential developed by Ioannidou et al. [14], this force field incorporates the strength anisotropy fundamental to the colloidal C-S-H system. This allows for an accurate interpretation of the cohesive and frictional behaviors between the C-S-H colloids. Fig. 1 illustrates the basic interactions between two C-S-H colloids as captured by the CFFF. The two colloids, labelled i and j, experience a net normal force potential $F_n(r)$ and tangential force potential $F_t(r)$. The normal force $F_n(r)$ is a function of particle separation r, given by

$$F_n(r) = \frac{k(r-D_0)}{D_0}\left[1 + e^{\alpha\left(\frac{r-D_0}{D_0\varepsilon_\mu}-1\right)}\right]^{-1} \tag{1}$$

where $k = \pi E D_0 D_e(1+e^{-\alpha})/4$ is a particle size-dependent parameter, D_0 is the average particle diameter, α is a fitting parameter (= 1.55) measured from the atomistic C-S-H layered structure, E is the elastic constants of atomistic C-S-H layered structure, and $D_e = 2D_iD_j/(D_i+D_j)$ is the harmonic mean of particles D_i and D_j.

The maximum value of $F_t(r)$ is limited by the interfacial shear strength, defined by $\mu F_n(r)+F_c(r)$. It can be expressed as

$$F_t(r) = \min\left[F_s(r), \mu F_n(r)+F_c(r)\right] \tag{2}$$

where $F_s(r)$ is the sliding force that is a function of the contact radius a between interacting colloids, given by

$$F_s(r) = 8\Delta_t G_e a \tag{3}$$

where Δ_t is an increment of tangential displacement, $G_e = G/2(2-v)$ for two colloids with the same shear modulus G and Poisson's ratio v, and $a = a_0 + \sqrt{D_e(D_0 - r)/4}$ where a_0 is the contact radius at force equilibrium and $\sqrt{D_e(D_0 - r)/4}$ describes the geometrical component for elastic compression of contacting colloids; and $F_c(r)$ is the cohesive force between two particles when $F_n(r) = 0$, which is related to the cohesive strength c between two colloids and the radius of contact a between colloids, yielding

$$F_c(r) = 8\pi c a^2 \tag{4}$$

As only non-bonded interactions exist between the C-S-H colloids and the nano-indenter, the Lennard-Jones potential was employed to describe their interactions, given by

$$E_{nonbond}(r_{ij}) = 4\varepsilon_{ij}\left[(\frac{\sigma_{ij}}{r_{ij}})^{12} - (\frac{\sigma_{ij}}{r_{ij}})^{6}\right] \tag{5}$$

where r_{ij} is the distance between the C-S-H colloids and the atoms of nano-indenter, ε_{ij} is the depth of the potential well (set to 10), and σ_{ij} is the distance at which the potential energy E is zero. In addition, it should be noted that the interaction within the nano-indenter was ignored as it was set to be a rigid body.

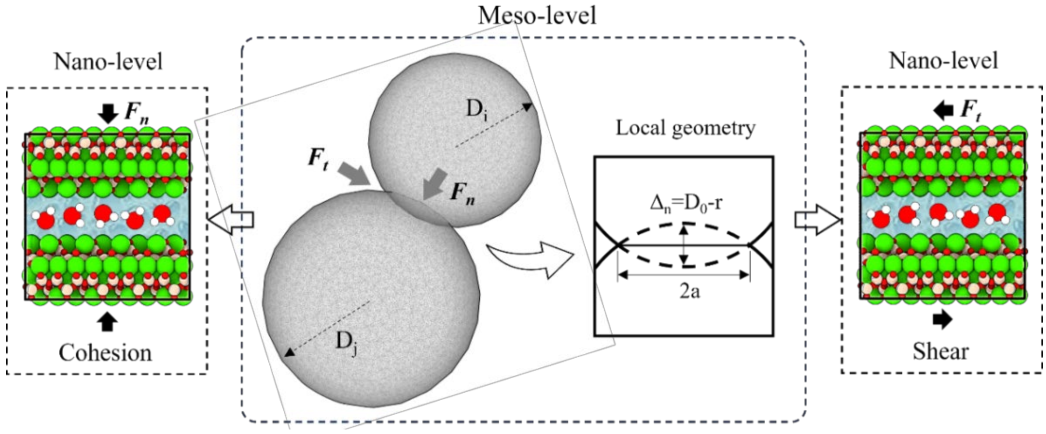

Fig. 1 Schematic view of the fundamental interactions between two C-S-H colloids, as captured by the cohesive-frictional force field (CFFF).

2.2 Model construction

The CG models of C-S-H, each measuring 0.5 μm × 0.5 μm × 0.3 μm, were constructed based on the polydisperse assembly of C-S-H colloids. The implementation of polydispersity was employed according to the method proposed in Ref. [18], where the colloid diameter ranges from a minimum of 3.0 nm to a maximum of 15.0 nm, with a mean of 5.0 nm. The particle size distribution (PSD) followed a Gaussian distribution, as depicted in Fig. 2(a). The packing density of C-S-H is defined as $\eta = V_s/V$, where $V_s = \sum_{i=1}^{N} \frac{\pi D_i^3}{6}$ represents the total volume of N colloids in the system and V is the volume of the simulation box. Given the variability in the packing density of C-S-H as measured from experiments [19, 20], three different packing densities (η = 0.50, 0.55, and 0.60) were considered. Following the construction of the C-S-H meso-structures, an exposed surface was created by introducing a 0.7 μm vacuum along the z-direction. A conical indenter, comprising 21381 atoms and constructed using a diamond molecular structure, was then placed on top of the C-S-H substrate. The tip of the indenter was positioned 0.3 μm away from the surface of the C-S-H substrate. The indenter's top and bottom radii were 100 nm and 10 nm, respectively (to consider the wear effect), and its height was 100 nm. Fig. 2(b) provides a schematic view of the meso-model setup for the nanoindentation.

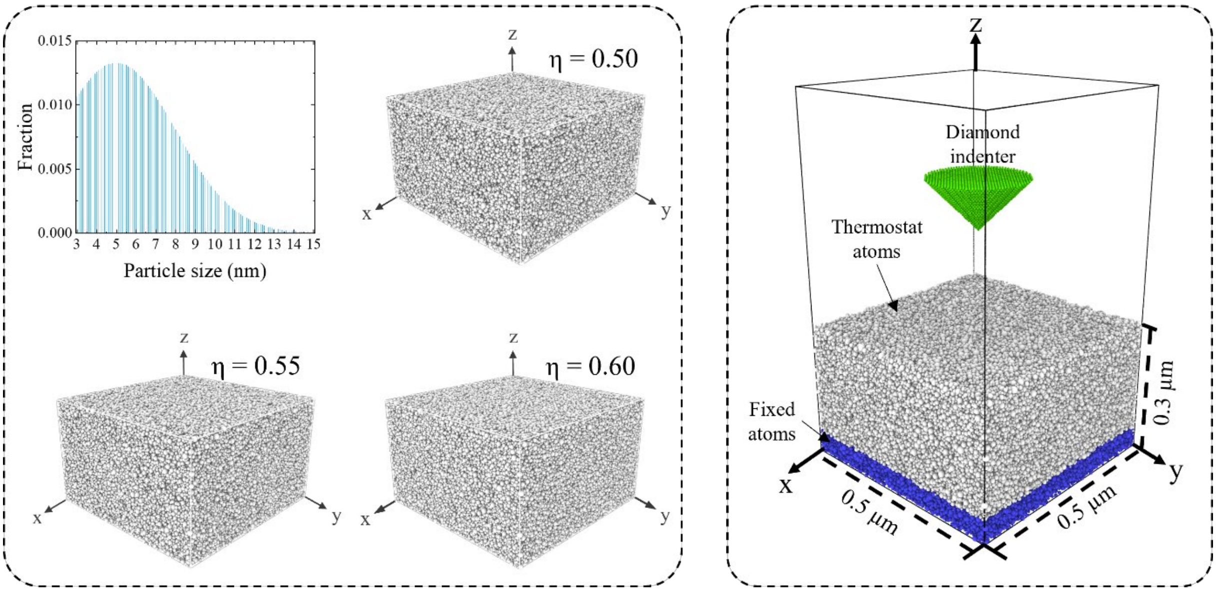

(a) (b)

Fig. 2 (a) Gaussian distribution implemented for the construction of the C-S-H meso-structure using various colloid sizes, and the constructed meso-structure of C-S-H with the packing densities of 0.50, 0.55 and 0.60; (b) the set-up of the C-S-H meso-model for the nanoindentation test.

2.3 Simulation details

The colloid coordinates and box dimensions in the *x* and *y* direction were first relaxed using the energy minimization technique, with a convergence criterion of 10^{-6} kcal/mol. Then the packed colloidal systems were equilibrated for 10 ns under an isothermal-isobaric (NPT) ensemble. The Nose-Hoover thermostat and barostat algorithms were used for the temperature (300 K) and pressure (101 kPa, atmospheric pressure) control [21]. To investigate the meso-mechanics using the designed nano-indenter, the indenter was manipulated to move towards the C-S-H substrate with a constant speed (1.0 Å/ps) under a canonical (NVT, 300K) ensemble. The nanoindentation process comprised three stages: (1) the nano-indenter made contact with the C-S-H surface and began to penetrate the C-S-H substrate; (2) the nano-indenter reached the maximum depth (50, 75 or 100 nm) and maintained its position for a certain period (0 ns and 0.5 ns); (3) the nano-indenter was retracted with a constant speed (1.0 Å/ps) until it left the C-S-H surface. During the nanoindentation process, the energy minimization technique was implemented after each step to achieve a stable configuration. The force exerted on the nano-indenter was recorded at each step, along with its penetration depth.

All the simulations were performed using the Large-scale Atomic/Molecular Massively Parallel Simulator (LAMMPS) package. Periodic boundary conditions were applied in all directions of the structures throughout all the simulation processes mentioned above.

3. Results and Discussion

3.1 Load-displacement curve

During the indentation process, various parameters such as load and penetration depth can be measured [22, 23]. These values can be graphed to create load-depth curves, which can be used to determine the mechanical properties of the material. In this study, the recorded displacement of the nano-indenter did not represent the actual penetration depth. The contact point, where the nano-indenter first made contact with the C-S-H substrate, needed to be identified first. Fig. 4(a) shows a typical load-displacement curve of the nano-indenter on the C-S-H substrate (η=0.50). As the nano-indenter approached the C-S-H substrate, a negative load was observed due to the attraction between the nano-indenter and the substrate. This load increased with displacement until it reached its maximum, after which the nano-indenter began to make contact with the substrate and the load gradually became positive. The point where the load transitioned from negative to positive was defined as the contact point, as labelled in Fig. 4(a), which agrees with the definition used in experimental and simulation studies [10, 24].

Once the contact point was identified, the penetration depth could be calculated from this point forward. Fig. 4(b-d) plots the load-depth curves for the nanoindentation tests performed on three colloidal C-S-H substrates (η=0.50, 0.55 and 0.60). During the penetration stage, the load continued to increase as the nano-indenter penetrated deeper into the substrates [25]. The calculated indentation harness (H), defined as the maximum load (F_{max}) divided by the residual indentation area (A_r), was 0.55, 1.16 and 2.63 GPa, respectively. This suggested that the hardness of packed C-S-H colloids was positively correlated with their packing densities. The fluctuation in load during indentation could be attributed to the local rearrangements (e.g., debonding, rebonding, and sliding) of the colloids. Furthermore, the slope of the load-depth curves increased with penetration depth, indicating that the rearrangements of the colloids resulted in a denser and harder system. During the retraction stage, all colloidal C-S-H substrates displayed similar unloading curves, with the force decreasing significantly in a short period. This indicates that the indentation led to the plastic deformation of the C-S-H substrates, resulting in the nano-indenter rapidly losing contact with numerous colloids of the substrate upon unloading. The load decreased to a negative value after several steps, indicating that the interaction between the nano-indenter and the C-S-H substrate changed from repulsion to attraction as the penetration depth decreased. The load then gradually increased to zero until the indenter was completely removed from the C-S-H substrate. Compared to the unloading curves obtained by experiments, the slope (*dF/dh*, an indication of the residual elastic modulus [26]) of the simulated curves was noticeably larger. This is because in experiments the penetration depth is much smaller than the height of the samples, leaving a certain height of unpenetrated C-S-H gel in the elastic stage.

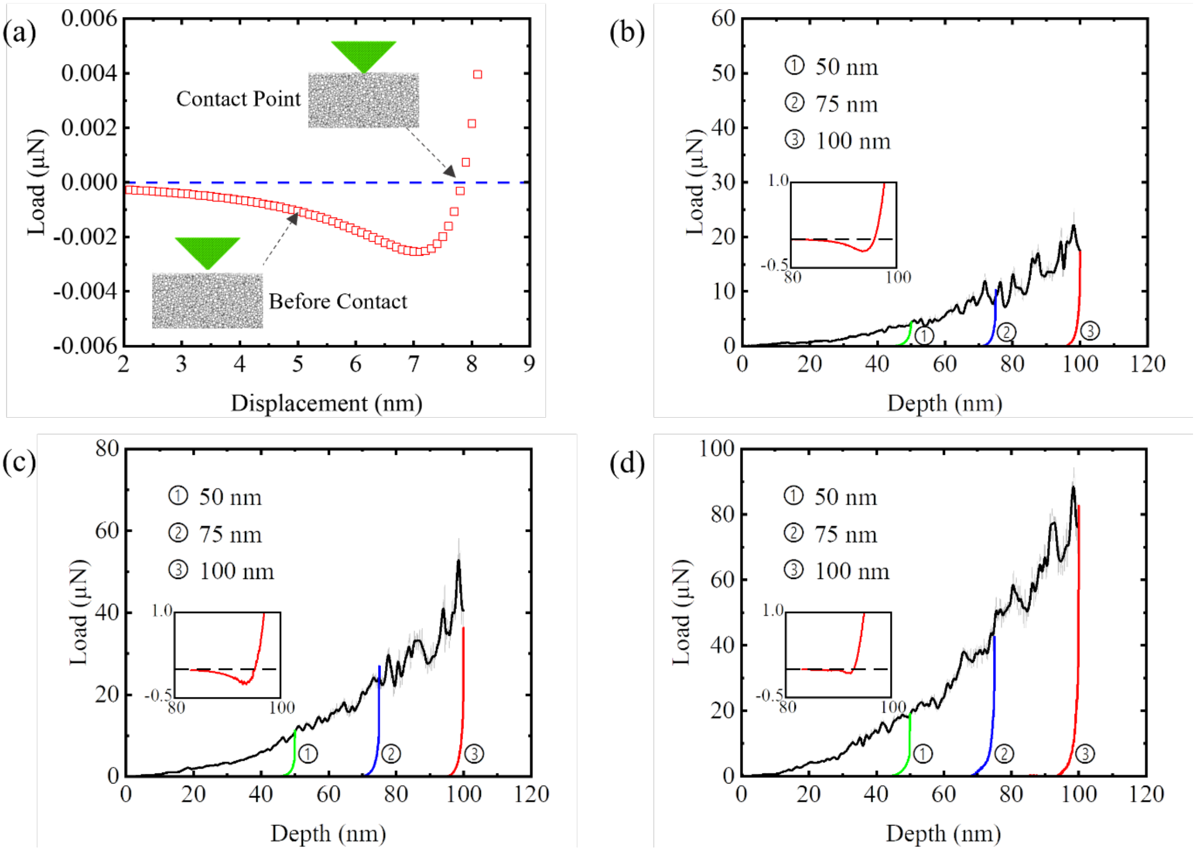

Fig. 3 (a) Typical load-displacement curves obtained from nanoindentation simulation at the initial stage; (b-d) the penetration and retraction curves at different indentation depths (50, 75, and 100 nm) for the packed C-S-H colloids with the packing densities of 0.50, 0.55 and 0.60.

3.2 Structural analysis

One of the key advantages of MD simulation is its ability to provide a detailed view of the formation and progression of plasticity in the C-S-H substrate during nano-indenter penetration [27-29]. Fig. 4 illustrates the displacement vectors and shear strain nephograms of the colloids in two C-S-H substrates (η = 0.50 and 0.60) at various penetration depths (40, 60, 80, and 100 nm). As the nano-indenter penetrated the C-S-H substrates, the surrounding colloids shifted from their original positions, primarily in a direction perpendicular to the nano-indenter's surface [24]. The deeper the nano-indenter penetrated, the larger the displacement of these C-S-H colloids. There were two main differences between the two packed C-S-H colloidal systems (η = 0.50 and 0.60). Firstly, in the colloidal system (η = 0.50), the displaced colloids were spread over a wide range, while in the system (η = 0.60), the displaced colloids were concentrated around the nano-indenter at the same penetration depth. This was because the low-density system had a loose structure, and all colloids were potentially affected by the stress induced by nanoindentation. In contrast, in a high-density system, the colloids were relatively stable, and only those around the nano-indenter experiencing high stress could be disturbed. Secondly, in the colloidal system (η = 0.50), the colloids at different depths move downward during the nanoindentation process, while in the system (η = 0.60), the colloids near the surface move laterally and those at greater depths moved downward. This suggested that the colloids in the high-density system were not easily compressed by the nano-indenter due to its low porosity, and were instead squeezed to the sides.

As the penetration depth increased, the region experiencing local shear strain gradually expanded and the strain value also increased (see the evolution of light blue, green, and red colloids in Fig. 4a and 4b) [24]. Comparing the two colloidal systems (see the distribution of red colloids in Fig. 4a and 4b), the high-strain colloids in the low-density system were concentrated at the nano-indenter's tip, while those in the high-density system were dispersed at various depths around the nano-indenter. Moreover, in the low-density colloidal system, the colloids around the nano-indenter at shallow depths exhibited negligible shear strain, while in the high-density system, colloids in the same region showed significant shear strain. These differences between the two systems suggested that the colloids in the low-density system were easily compressed without causing deformation in the surrounding regions at low depths, while those in the high-density system were easily displaced to the sides, causing the deformation in the surrounding regions at low depths. This squeezing process resulted in high shear strain in the impact regions, a phenomenon that aligned with the observations made from the displacement vectors.

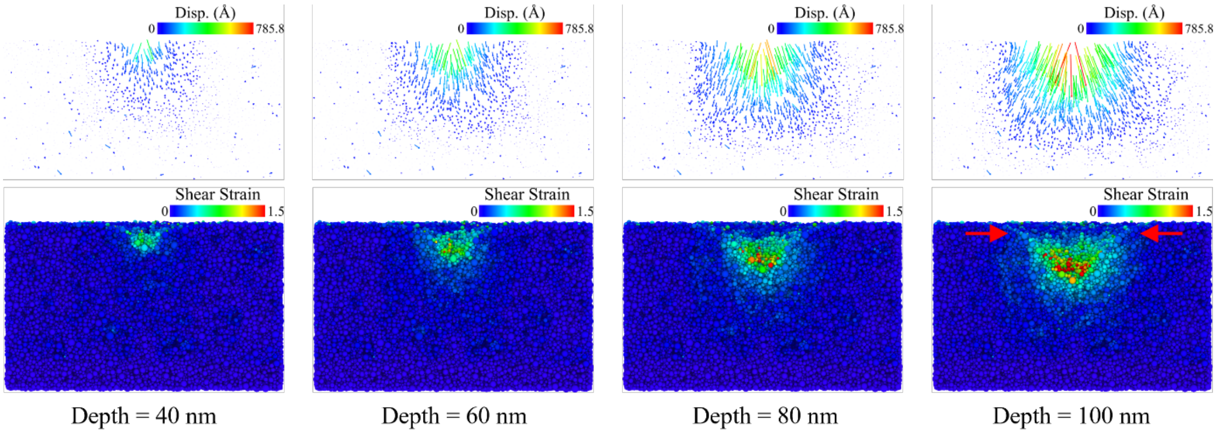

(a) Packing density = 0.5

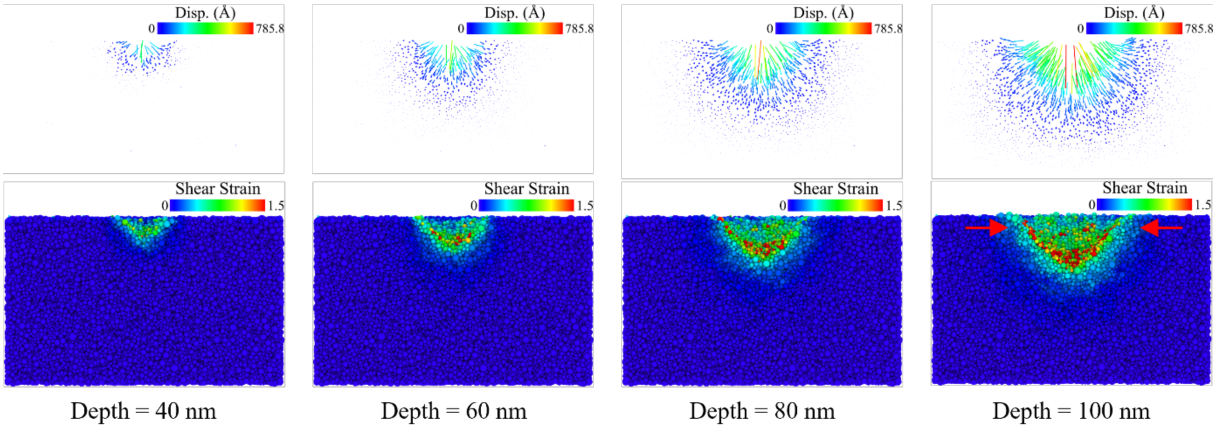

(b) Packing density = 0.6

Fig. 4 (a) Displacement vectors and shear strain nephograms of the colloids in the C-S-H substrate (η = 0.50) during the penetration process; (b) displacement vectors and shear strain nephograms of the colloids in the C-S-H substrate (η = 0.60) during the penetration process. The red arrows were used to point out the difference between the surrounding regions at low depths of the low-density and high-density C-S-H.

To gain further insight into the structural evolution of the colloidal C-S-H systems during the nanoindentation process, the density increase map and the local density profile as a function of distance along the vertical direction of the nano-indenter's surface were recorded, as depicted in Fig. 5. The density increase map revealed that following penetration, the density around the nano-indenter noticeably increased. As the packing density increased, the level of density increase was reduced. This was attributed to the fact that a high-porosity system easily concentrated the colloids around the nano-indenter, while a low-porosity system behaved the opposite. Additionally, it was observed that for the low-density system, the density increase in regions distant from the nano-indenter was not uniform after the penetration process. However, as the packing density increased, the density increase in these regions became more uniform. This was because these local regions, despite being distant from the nano-indenter, were still easily influenced by the stress induced by the nano-indenter, as evidenced by the displacement vectors in Fig. 3(a). From the local density profiles, a low-density region was identified near the nano-indenter. Outside this region, a high-density region was observed, as shown in Fig. 5(b). Within this region, the density gradually decreased with the increase in distance from the surface of the nano-indenter, until it reached the bulk density. As the penetration depth increased, the low-density region contracted, while the high-density region expanded and became denser. These contraction and expansion phenomena gradually diminished as the packing density increased. Comparing the three systems, it was found that a system with a lower density had a larger impact region (comprising both low and high-density regions) at the same penetration depth. For example, the impact region of low-density C-S-H (η = 0.50) was 118 nm and 150 nm respectively at penetration depths of 50 nm and 100 nm, while that of high-density C-S-H (η = 0.60) was 106 nm and 140 nm at the same penetration depths. This indicated that the nano-indenter had a longer range of effect on the low-density system.

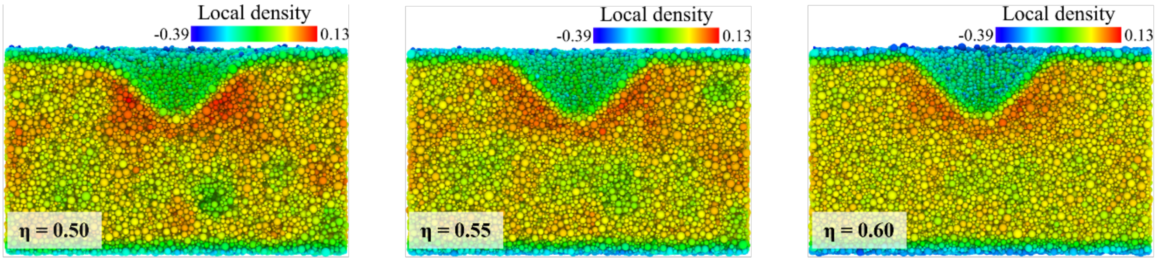

(a) Density increase map

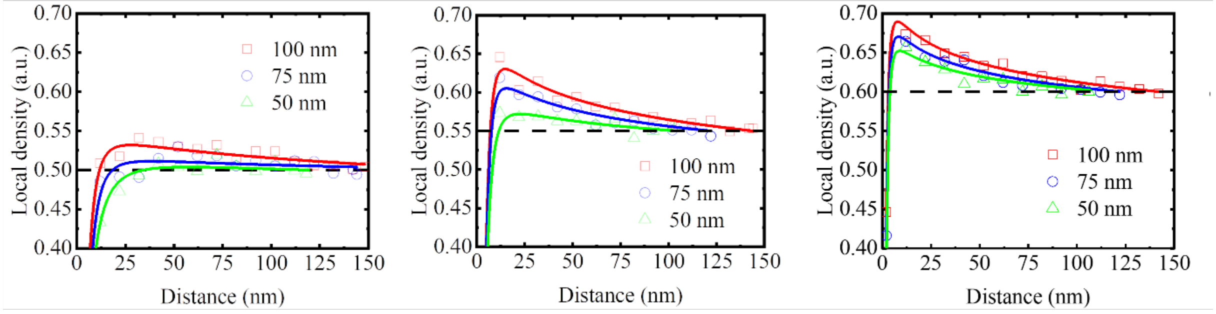

(b) Local density profile

Fig. 5 (a) Density increase map of the packed colloidal C-S-H systems (η = 0.50, 0.55 and 0.60) at a penetration depth of 100 nm; (b) Local density profile for the packed colloidal C-S-H systems (η = 0.50, 0.55 and 0.60) as a function of displacement, measured vertically from the surface of the nano-indenter at varying penetration depths.

3.3 Stress relaxation

Stress-relaxation tests involve the application of a constant deformation, specifically a constant indentation depth, to a material [30, 31]. These tests measure the relaxation of stress beneath the indenter by monitoring the load required to maintain a constant depth. In this study, the stress-relaxation behavior of the packed colloidal C-S-H systems was measured at three different penetration depths (i.e., 50, 75 and 100 nm) for a constant period of 0.5 ns, after which the nano-indenter was extracted with a speed of 1.0 Å/ps, as shown in Fig. 6(a). The results indicated that there was a significant decrease in the load exerted on the nano-indenter during the stress-relaxation process. This suggested that the nanoindentation process destabilized the colloidal system, prompting the colloids to adjust their positions to stabilize the system [32]. Notably, after the initial rapid decrease, the high-density systems (η = 0.55 and 0.60) underwent a second-stage evolution, where the force on the nano-indenter decreased at a much slower rate, corresponding to the viscous characteristics of C-S-H [33, 34]. This stage appeared at 0.61 ns, 0.92 ns, and 1.22 ns for the system (η = 0.55) and at 0.61 ns, 0.90 ns, and 1.19 ns for the system (η = 0.60) at penetration depths of 50, 75, and 100 nm, respectively. This indicated that the colloidal systems with a higher penetration depth or a lower packing density require more time to stabilize. Fig. 6(b) displays the local density profiles for the three colloidal C-S-H systems after the stress relaxation at a penetration depth of 100 Å. For the low-density system (η = 0.50), the local density within the 75 Å region near the nano-indenter increased after the stress relaxation, while beyond this region, the local density remained unchanged. It proved that the loose structure was compacted to be denser near the nano-indenter after the stress relaxation process [35]. For the high-density systems (η = 0.55 and 0.60), the local density profile had ignorable changes after the stress relaxation. This implied that the dense structure was not compacted by the stress relaxation, and the system's stress release was achieved through minor adjustments of the colloids.

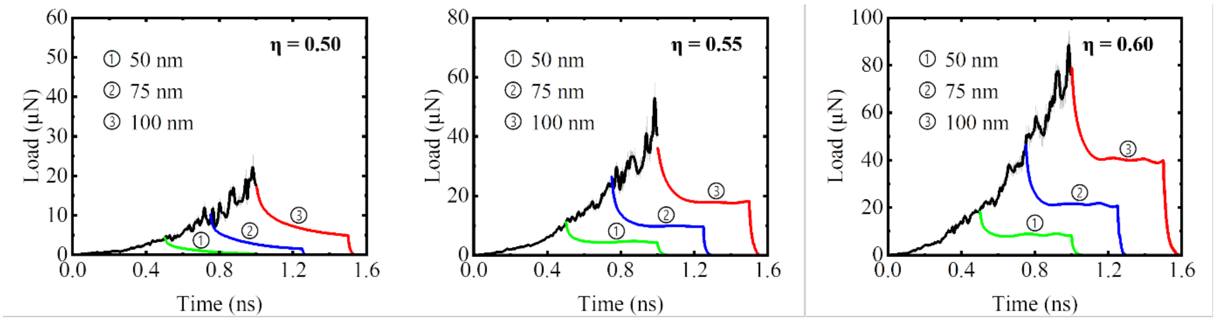

(a) Load vs time curves

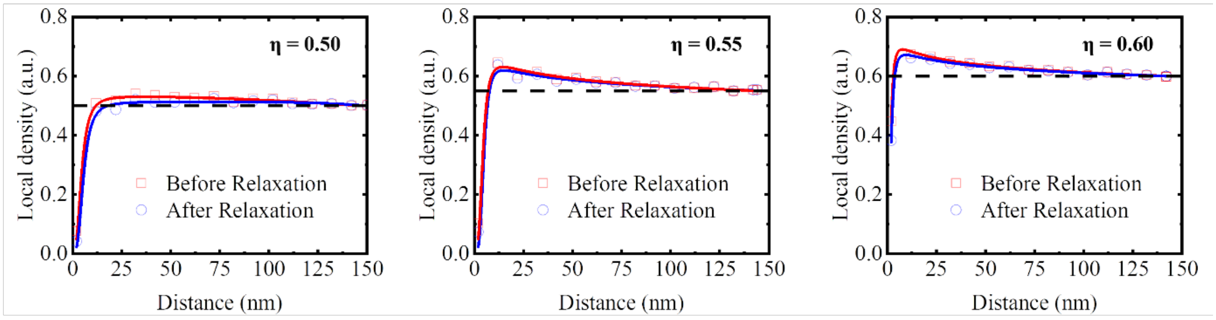

(b) Local density profile

Fig. 6 (a) Load vs time curves during the nanoindentation process, which involved a 0.5 ns period to relax the colloidal systems (η = 0.50, 0.55 and 0.60) at three different penetration depths (50, 75 and 100 nm); (b) Local density profile for the packed colloidal C-S-H systems (η = 0.50, 0.55 and 0.60) before and after the stress relaxation process.

Fig. 7 illustrates the evolution of the stress distribution map of the colloidal C-S-H systems (η = 0.50, 0.55 and 0.60) before and after the stress relaxation at a penetration depth of 100 Å. The results indicated that the nanoindentation process led to concentrated stress on some colloids, primarily near the nano-indenter. As the packing density of C-S-H increased, more colloids bore high levels of both compressive and tensile stress, and these high-stress colloids were distributed over a larger range. After the stress relaxation, these colloids released the high stress they were subjected to. In the low-density system (η = 0.50), nearly all colloids that experienced high stress managed to release it. However, in the high-density system (η = 0.60), many colloids continued to endure high stress even after stress relaxation. The difference between the low- and high-density systems was attributed to the varying flexibility of the colloids. Colloids in a low-density system exhibited greater flexibility, enabling them to adjust their positions more effectively to alleviate their stress.

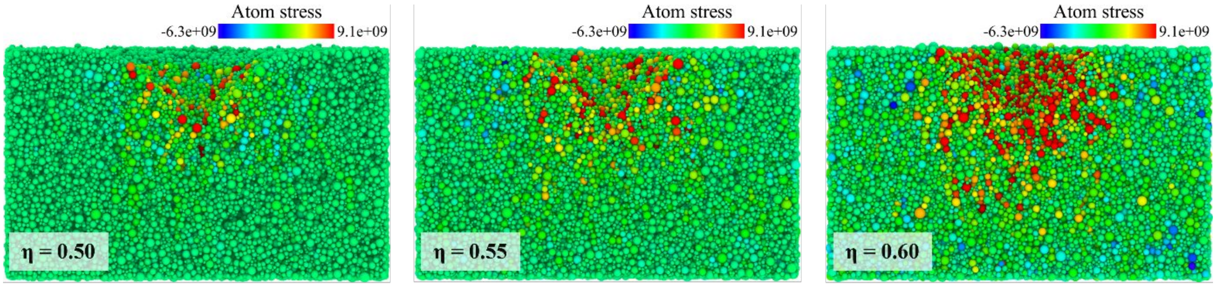

(a) Before Relaxation

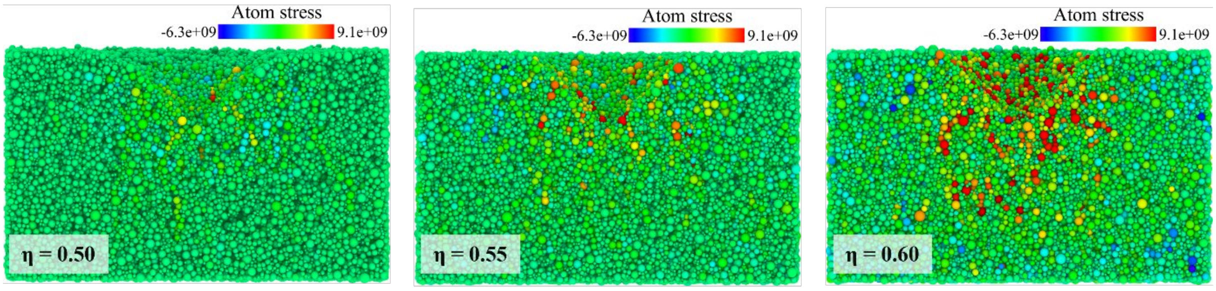

(b) After Relaxation

Fig. 7 (a) Stress distribution map of the colloidal C-S-H systems (η = 0.50, 0.55 and 0.60) after the penetration process reached a depth of 100 Å; (a) Stress distribution map of the colloidal C-S-H systems (η = 0.50, 0.55 and 0.60) after the stress relaxation at a constant penetration depth of 100 Å.

3.4 Impact of loading rate

The loading rate significantly influences the meso-mechanics of the colloidal C-S-H system during the nanoindentation process [36, 37]. To examine the effect of the loading rate, two additional rates (0.5 Å/ps and 1.5 Å/ps) were considered in this study. The penetration process was carried out until a depth of 100 nm was reached, after which the nano-indenter was held at this depth for 0.5 ns to observe stress relaxation. Subsequently, the nano-indenter was extracted at a speed of 1.0 Å/ps. Fig. 8(a) depicts the load versus time curves throughout the entire simulation process. During the penetration process, a high loading rate resulted in a rapid increase in the load exerted on the nano-indenter and fluctuating load-displacement curves. Such fluctuation indicated that the colloidal systems frequently experienced instability during the penetration process [38]. Moreover, the lower the system's density, the more fluctuation was observed in the curves. On the contrary, a low loading rate led to a minor increase in the load and smooth load-displacement curves, proving the colloidal systems underwent a relatively stable deformation process. During the stress-relaxation process, the load decreased more rapidly for the colloidal systems penetrated using a high loading rate, as the high loading rate made the system more unstable. Additionally, the load level after the first-stage stress relaxation was lower, and the occurrence of the second-stage stress relaxation was delayed for systems penetrated using a high loading rate. Fig. 8(b) shows the differences in the local density profiles of the colloidal systems after the nanoindentation process with high and low loading rates. Obviously, an increase in loading rate resulted in a denser region near the nano-indenter after the nanoindentation process. However, as the packing density increased, the influence of the loading rate on the local density profiles diminished. This revealed that the structural evolution of the low-density system was more sensitive to the loading rate of the nanoindentation test [35, 39]. In addition, the impact region was almost not affected by the loading rates.

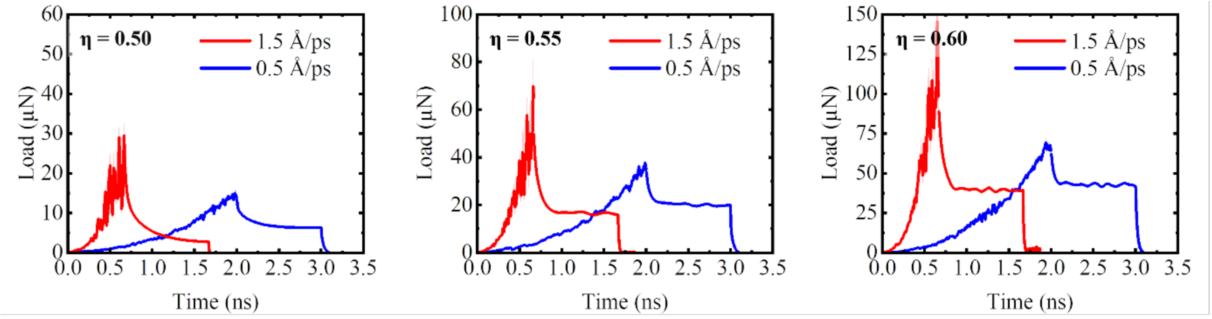

(a) Load vs time curves

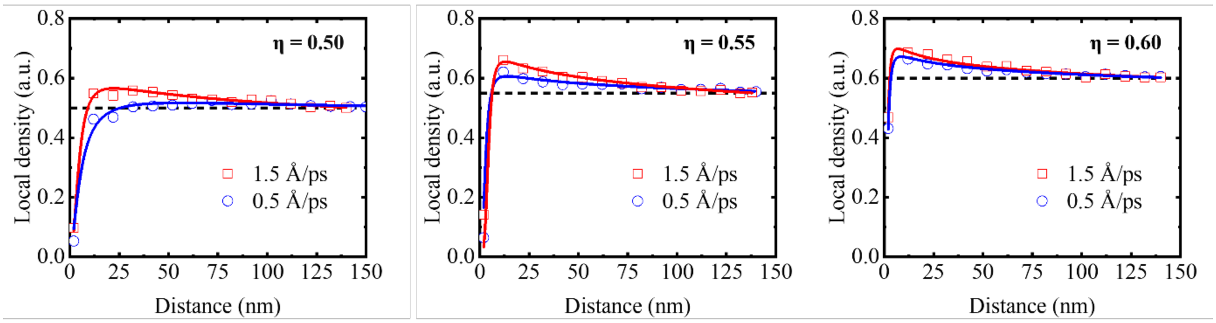

(b) Local density profile

Fig. 8 (a) Load vs time curves for colloidal C-S-H systems (η = 0.50, 0.55 and 0.60) during the nanoindentation process using two different loading rates (0.5 Å/ps and 1.5 Å/ps). The penetration depth was 100 nm and the stress relaxation lasted for 0.5 ns; (b) Local density profile before and after the stress relaxation process.

Fig. 9 presents the stress distribution map of the C-S-H colloidal systems (η = 0.50 and 0.60) after the stress relaxation at a penetration depth of 100 Å. The results indicated that an increase in the loading rate accelerated the formation of high-stress colloids, as evident in Fig. 9(a1) and Fig. 9(b1). It was attributed to the fact that a high loading rate left less time for the colloids to adjust their positions to alleviate their stress. It was also observed that high-stress colloids were distributed over a wider range in the colloidal systems under a low loading rate, while those under a high loading rate were more concentrated near the nano-indenter. This observation aligned with their respective density distribution profiles (Fig. 8b). After the stress relaxation, regardless of the loading rate, the system with a packing density of 0.5 had virtually no high-stress colloids remaining. However, in the systems with packing densities of 0.55 and 0.60, some colloids remained under high stress after stress relaxation. The difference between different loading rate cases was that high-loading rate cases had fewer high stress colloids after stress relaxation. It agreed with the observation in Fig. 8(a) those systems with high-loading rates experienced a faster decrease in load. These results confirmed that although a high loading rate initially made the colloidal system more unstable (with more high-stress colloids) after the nano-indenter's penetration process, the colloidal system became more stable after stress relaxation.

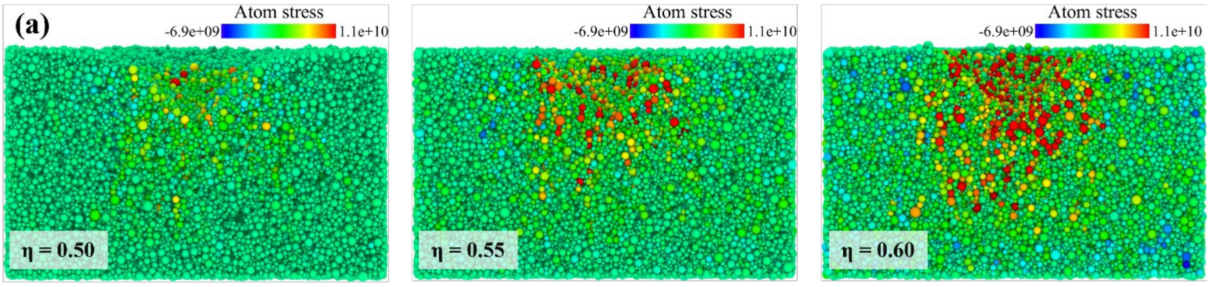

(1) Before Relaxation

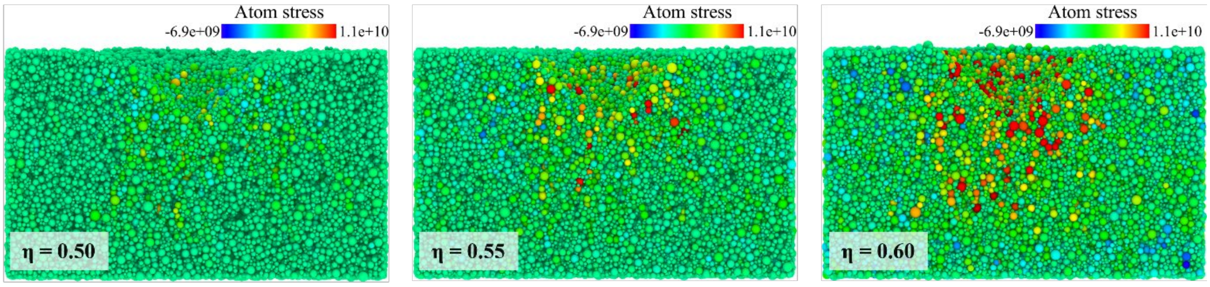

(2) After Relaxation

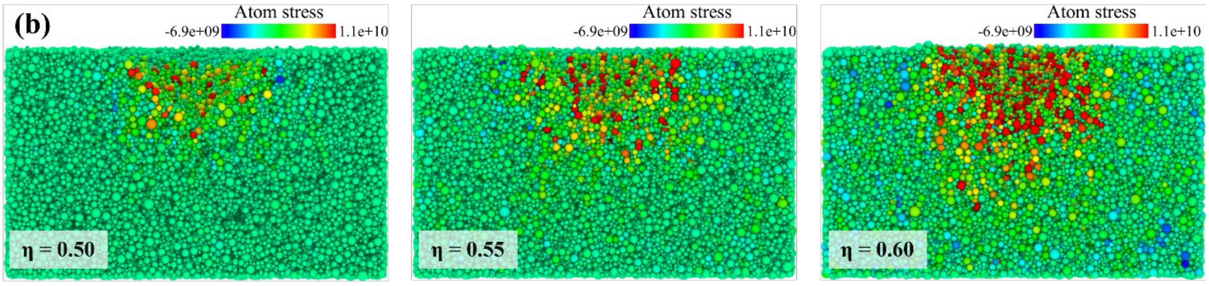

(1) Before Relaxation

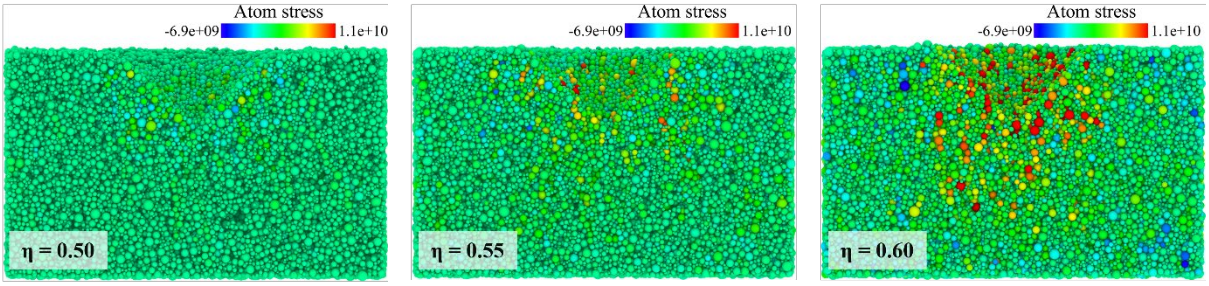

(2) After Relaxation

Fig. 9 Stress distribution map after the stress relaxation of the colloidal C-S-H systems (η = 0.50, 0.55 and 0.60) that were penetrated using the loading rate of (a) 0.5 Å/ps and (b) 1.5 Å/ps.

4. Conclusions

In this work, the coarse-grained (CG) models for C-S-H colloidal particles with different packing densities (η = 0.50, 0.55 and 0.60) were established and meso-mechanically assessed via nanoindentation. The following conclusions can be drawn from the coarse-grained MD simulations:

(1) The load-depth curves from the nanoindentation tests on the colloidal C-S-H substrates mirrored experimental results. The calculated indentation harness was 0.55, 1.16 and 2.63 GPa respectively for the colloidal systems with packing densities of 0.50, 0.55, and 0.60 at the loading rate of 1.0 Å/ps. The fluctuation in load-depth curves was attributed to the local rearrangements of the colloids, which resulted in a denser and harder system. Moreover, the indentation caused plastic deformation of the colloidal C-S-H, with the nano-indenter quickly losing contact with many substrate colloids upon unloading.

(2) Structural analysis revealed that the displacement of C-S-H colloids increased with the penetration depth. The colloids in low-density systems were easily compressed and spread over a wider range, while those in high-density systems were more stable and concentrated around the nano-indenter. The high-density systems were not easily compressed due to low porosity and were instead squeezed to the sides, causing deformation in the surrounding regions at low depths. In addition, the nano-indenter had a broader impact on low-density C-S-H (η = 0.5, impact radius = 118 and 150 nm respectively at indentation depths = 50 and 100 nm) than high-density C-S-H (η = 0.6, impact radius = 106 and 140 nm at the same depths).

(3) Packed C-S-H colloids exhibited stress relaxation behavior. The first stage saw a significant load decrease on the nano-indenter, indicating that the nanoindentation process destabilized the colloidal systems. Systems with a higher penetration depth or lower packing density took longer to stabilize. After the first stage, the load on the nano-

indenter decreased at a slower rate (second stage), suggesting that the colloids displayed viscous characteristics. In addition, the low-density structure densified near the nano-indenter, while changes in high-density systems were negligible.

(4) The loading rate significantly affected the meso-mechanics of the colloidal C-S-H system. High loading rates led to rapid load increases and fluctuating load-displacement curves, indicating unstable deformation. High loading rates also created a denser region near the nano-indenter and hastened the formation of high-stress colloids. However, after stress relaxation, systems with high loading rates became more stable, with fewer high-stress colloids remaining. Structurally, low-density systems were more sensitive to the loading rate. In addition, the impact region was almost not affected by the loading rates.

Declaration of competing interest

The authors declare that they have no known competing financial interests or personal relationships that could have appeared to influence the work reported in this paper.

Acknowledgments

This research was supported by Guangdong Province R&D Plan for Key Areas (Project code: 2019B111107002) , the Hong Kong Research Grants Council—Theme-based Research Scheme (Project code: T22-502/18-R), and the NSFC/RGC Joint Research Scheme (Project code: N_CityU542/20).

References

[1] M. Eftekhari, S. Mohammadi, Molecular dynamics simulation of the nonlinear behavior of the CNT-reinforced calcium silicate hydrate (C–S–H) composite, Composites Part A: Applied Science and Manufacturing 82 (2016) 78-87.

[2] M. Kai, L. Zhang, K. Liew, Graphene and graphene oxide in calcium silicate hydrates: Chemical reactions, mechanical behavior and interfacial sliding, Carbon 146 (2019) 181-193.

[3] M.-F. Kai, D.-S. Hou, F. Sanchez, C.-S. Poon, J.-G. Dai, Nanoscale Insights into the Influence of Seawater (NaCl) on the Behavior of Calcium Silicate Hydrate, The Journal of Physical Chemistry C 127 (2023) 8735-8750.

[4] S. Masoumi, D. Ebrahimi, H. Valipour, M.J. Abdolhosseini Qomi, Nanolayered attributes of calcium‐silicate‐hydrate gels, Journal of the American Ceramic Society 103 (2020) 541-557.

[5] J. Wang, S. Dong, S. Dai Pang, C. Zhou, B. Han, Pore structure characteristics of concrete composites with surface-modified carbon nanotubes, Cement and Concrete Composites 128 (2022) 104453.

[6] M.J.A. Qomi, L. Brochard, T. Honorio, I. Maruyama, M. Vandamme, Advances in atomistic modeling and understanding of drying shrinkage in cementitious materials, Cement and Concrete Research 148 (2021) 106536.

[7] S. Gautham, S. Sasmal, Recent advances in evaluation of intrinsic mechanical properties of cementitious composites using nanoindentation technique, Construction and Building Materials 223 (2019) 883-897.

[8] M. Li, H. Tan, X. He, S. Jian, G. Li, J. Zhang, X. Deng, X. Lin, Enhancement in compressive strength of foamed concrete by ultra-fine slag, Cement and Concrete Composites 138 (2023) 104954.

[9] C. Liu, X. Huang, Y.-Y. Wu, X. Deng, J. Liu, Z. Zheng, D. Hui, Review on the research progress of cement-based and geopolymer materials modified by graphene and graphene oxide, Nanotechnology Reviews 9 (2020) 155-169.

[10] W. Xu, Z. Tang, Y. Xie, G. Long, Z. Luo, M. Kai, G. Ma, S. Zaland, Recent advances and insights in nanoindentation technique in the characterization of cement-based materials, Journal of Building Engineering (2023) 108022.

[11] R.J.-M. Pellenq, A. Kushima, R. Shahsavari, K.J. Van Vliet, M.J. Buehler, S. Yip, F.-J. Ulm, A realistic molecular model of cement hydrates, Proceedings of the National Academy of Sciences 106 (2009) 16102-16107.

[12] D. Hou, H. Li, L. Zhang, J. Zhang, Nano-scale mechanical properties investigation of CSH from hydrated tri-calcium silicate by nano-indentation and molecular dynamics simulation, Construction and Building Materials 189 (2018) 265-275.

[13] H. Yin, X. Wang, H. Qin, S. Wang, K. Cai, Nanoindentation Study of Calcium-Silicate-Hydrate Gel via Molecular Dynamics Simulations, Nanomaterials 13 (2023) 2578.

[14] K. Ioannidou, K.J. Krakowiak, M. Bauchy, C.G. Hoover, E. Masoero, S. Yip, F.-J. Ulm, P. Levitz, R.J.-M. Pellenq, E. Del Gado, Mesoscale texture of cement hydrates, Proceedings of the National Academy of Sciences 113 (2016) 2029-2034.

[15] D. Hou, W. Zhang, M. Sun, P. Wang, M. Wang, J. Zhang, Z. Li, Modified Lucas-Washburn function of capillary transport in the calcium silicate hydrate gel pore: A coarse-grained molecular dynamics study, Cement and Concrete Research 136 (2020) 106166.

[16] R. Qin, A. Zhou, Z. Yu, Q. Wang, D. Lau, Role of carbon nanotube in reinforcing cementitious materials: An experimental and coarse-grained molecular dynamics study, Cement and Concrete Research 147 (2021) 106517.

[17] H. Liu, S. Xiao, L. Tang, E. Bao, E. Li, C. Yang, Z. Zhao, G. Sant, M.M. Smedskjaer, L. Guo, Predicting the early-stage creep dynamics of gels from their static structure by machine learning, Acta Materialia 210 (2021) 116817.

[18] S.D. Palkovic, S. Yip, O. Büyüköztürk, A cohesive-frictional force field (CFFF) for colloidal calcium-silicate-hydrates, Journal of the Mechanics and Physics of Solids 109 (2017) 160-177.

[19] L. Liu, C. Sun, G. Geng, P. Feng, J. Li, R. Dähn, Influence of decalcification on structural and mechanical properties of synthetic calcium silicate hydrate (CSH), Cement and Concrete Research 123 (2019) 105793.

[20] A.J. MacLeod, F.G. Collins, W. Duan, W.P. Gates, Quantitative microstructural characterisation of Portland cement-carbon nanotube composites using electron and x-ray microscopy, Cement and Concrete Research 123 (2019) 105767.

[21] M.-F. Kai, J.-G. Dai, Understanding geopolymer binder-aggregate interfacial characteristics at molecular level, Cement and Concrete Research 149 (2021) 106582.

[22] T. Fu, X. Peng, C. Wan, Z. Lin, X. Chen, N. Hu, Z. Wang, Molecular dynamics simulation of plasticity in VN (001) crystals under nanoindentation with a spherical indenter, Applied Surface Science 392 (2017) 942-949.

[23] K.E. Avila, V.H. Vardanyan, S. Küchemann, H.M. Urbassek, Response of an amorphous/crystalline interface to nanoindentation: an atomistic study, Applied Surface Science 551 (2021) 149285.

[24] Z. Du, X. Zhu, Y. Yuan, Molecular investigation on the adhesion and deformation behaviors of asphalt binder under nanoindentation, Construction and Building Materials 295 (2021) 123683.

[25] C. Hu, Z. Li, A review on the mechanical properties of cement-based materials measured by nanoindentation, Construction and Building Materials 90 (2015) 80-90.

[26] C. Hu, Y. Gao, Y. Zhang, Z. Li, Statistical nanoindentation technique in application to hardened cement pastes: Influences of material microstructure and analysis method, Construction and Building Materials 113 (2016) 306-316.

[27] J. Li, J. Guo, H. Luo, Q. Fang, H. Wu, L. Zhang, Y. Liu, Study of nanoindentation mechanical response of nanocrystalline structures using molecular dynamics simulations, Applied Surface Science 364 (2016) 190-200.

[28] H.-T. Luu, S.-L. Dang, T.-V. Hoang, N. Gunkelmann, Molecular dynamics simulation of nanoindentation in Al and Fe: On the influence of system characteristics, Applied Surface Science 551 (2021) 149221.

[29] D. Hua, W. Ye, Q. Jia, Q. Zhou, Q. Xia, J. Shi, Y. Deng, H. Wang, Molecular dynamics simulation of nanoindentation on amorphous/amorphous nanolaminates, Applied Surface Science 511 (2020) 145545.

[30] P. Patil, C. Jones, Stress Relaxation and Creep Nanoindentation for Cement Paste, Journal of Materials in Civil Engineering 36 (2024) 04023514.

[31] J. Frech-Baronet, L. Sorelli, J.-P. Charron, New evidences on the effect of the internal relative humidity on the creep and relaxation behaviour of a cement paste by micro-indentation techniques, Cement and Concrete Research 91 (2017) 39-51.

[32] H. Ye, A. Radlińska, Effect of alkalis on cementitious materials: Understanding the relationship between composition, structure, and volume change mechanism, Journal of Advanced Concrete Technology 15 (2017) 165-177.

[33] A. Morshedifard, S. Masoumi, M. Abdolhosseini Qomi, Nanoscale origins of creep in calcium silicate hydrates, Nature communications 9 (2018) 1785.

[34] M. Kai, L. Zhang, K. Liew, New insights into creep characteristics of calcium silicate hydrates at molecular level, Cement and Concrete Research 142 (2021) 106366.

[35] R. Hay, J. Li, K. Celik, Influencing factors on micromechanical properties of calcium (alumino) silicate hydrate C-(A-) SH under nanoindentation experiment, Cement and Concrete Research 134 (2020) 106088.

[36] S. Xu, Y. Feng, J. Liu, Q. Zeng, Micro indentation fracture of cement paste assessed by energy-based method: The method improvement and affecting factors, Construction and Building Materials 231 (2020) 117136.

[37] Y. Gan, C.R. Rodriguez, E. Schlangen, K. van Breugel, B. Šavija, Assessing strain rate sensitivity of cement paste at the micro-scale through micro-cantilever testing, Cement and Concrete Composites 121 (2021) 104084.

[38] E.S. Puchi-Cabrera, E. Rossi, G. Sansonetti, M. Sebastiani, E. Bemporad, Machine learning aided nanoindentation: A review of the current state and future perspectives, Current Opinion in Solid State and Materials Science 27 (2023) 101091.

[39] J. Xu, B. Wang, J. Zuo, Modification effects of nanosilica on the interfacial transition zone in concrete: A multiscale approach, Cement and Concrete Composites 81 (2017) 1-10.